Adsorption of fluoride using bimetallic oxide nanoparticles supported on industrial waste prepared by a chemical reduction method

A. Blanco-Flores[a,b], N.V. Arteaga-Larios[a], M.C. Ojeda-Escamilla[a], H.P. Toledo-Jaldin[c,d], G. López-Téllez[d], I. Rodríguez-Torres[a,*]

[a]*Instituto de Metalurgia-Facultad de Ingeniería, Universidad Autónoma de San Luis Potosí, Av. Sierra Leona 550, Lomas 2a sección, 78210 San Luis Potosí, San Luis Potosí, México, emails: learsi@uaslp.mx (I. Rodríguez-Torres), blancoflores81@hotmail.com (A. Blanco-Flores), narteaga@uaslp.mx (N.V. Arteaga-Larios), ojedaesc@uaslp.mx (M.C. Ojeda-Escamilla)*
[b]*División de Mecánica, Tecnológico de Estudios Superiores de Tianguistenco, Carretera Tenango-Marquesa km 22, Santiago Tilapa, 52650 Santiago Tianguistenco, Estado de México, México*
[c]*Facultad de Química, Universidad Autónoma del Estado de México, Paseo Tollocan y Paseo Colón, 50110 Toluca, Estado de México, México, email: helenpao@hotmail.com*
[d]*Centro Conjunto de Investigación en Química Sustentable UAEM-UNAM, (CCIQS), Carretera Toluca-Atlacomulco km 14.5, Unidad El Rosedal, 50200 Toluca, Estado de México, México, email: glopezt@uaemex.mx (G. López-Téllez)*

ABSTRACT

Steel slags (SSs) were used as support materials for Al-Cu oxide nanoparticles (Nps) for fluoride adsorption. The nanocomposites were prepared by a chemical reduction method and characterized by scanning electron microscopy, transmission electron microscopy, X-ray diffraction, pH_{zpc}, and surface area, although the surface area did not influence the deposition of nanoparticles. The interactions between the Al-Cu Nps and the waste were identified by X-ray photoelectron scanning (XPS) analysis. In SST, the Nps surrounded the grain boundary. The ferric phases in SSLP limited the deposition of Nps. Al Nps were deposited in larger amounts than Cu Nps. The characteristics of the waste were analyzed to establish the extent to which it can be applied as a support material. The nanocomposites showed better adsorption capacity than did the wastes. The kinetics of the nanocomposites was described by models that were different from those that had been fitted to the kinetic data for SST and SSLP. The equilibrium times for SSLP/Al–Cu and SST/Al–Cu were 380 and 130 min, respectively. The process was described as physisorption for SSLP/Al–Cu and chemisorption for SST/Al–Cu. The rate-controlling step was different before and after modification. The adsorption process for SST and SSLP took place on a heterogeneous surface. Removal by SST/Al–Cu was achieved through a combination of mechanisms. The adsorption efficiency of SST/Al–Cu was studied by modeling batch adsorbers. The most efficient system was the counterflow design. The material with the highest affinity for fluoride was SST/Al–Cu (5.25 mg g^{-1}).

Keywords: Al–Cu oxide nanoparticles; Industrial waste; Fluoride; Adsorption mechanism; Adsorber design; XPS analysis

1. Introduction

The synthesis of nanoparticles is a process that has been extensively used to obtain new materials. There are many methods of synthesis, such as sonochemistry, reduction, co-precipitation, microwave irradiation, laser treatment, and plasma treatment. Some of these methods are very specific, require expensive, special conditions and can generate wastes. For these reasons, researchers have focused on new methods of synthesis. New methods need to be

* Corresponding author.

environmentally friendly, reproducible, easy to maintain and feasible. In addition, these methods must be easily implemented for scaling. The chemical reduction method is described as easy, cost-effective, and efficient. Metal and metal-oxide nanoparticles have been synthesized by chemical reduction due to easy handling and economical aspects of the method [1].

Metal and metal-oxide nanoparticles can be applied in diverse fields, such as information storage, optoelectronics, sensors, fuel cell technology, catalysis, and adsorption processes [2,3]. These kinds of nanoparticles tend to aggregate because of their high surface energy; therefore, an alternative approach to stabilize these particles is to include them as part of a nanocomposite. The selection of a suitable support material is an important step in improving the effectiveness of applications in environmental fields [4]. Often, the use of activated carbon [5], zeolites [6], clays [7], graphene [8], and metal-organic derivatives [9] is common. However, these materials have several disadvantages, such as difficult routes of synthesis or treatment, low efficiency or limited pH operating ranges. Therefore, it is necessary to study other materials. Waste byproducts are a good alternative since they are cheap and easy to obtain. Steel slag (SS) is a byproduct of steel making and is produced during the separation of molten steel from impurities in steel-making furnaces. Because SS is generated in large quantities, its final deposition could become an environmental issue [10]. SS is composed of calcium, magnesium, iron, silicon oxides, Ca silicates, Ca-Al ferrites, and Fe spinels. The composition depends on the type of furnace, the initial raw material used in the process, the process operating conditions and the desired grade of steel purity. All phases and characteristics of materials are very important for their use as potential adsorbents [11]. During steel production, two kinds of SS can be generated: white and black SS. The chemical compositions of these materials are different because they are byproducts of two specific stages of steel processing [12]. Other researchers have previously used this kind of waste as an adsorbent material in dye, nickel, phosphorous and lead removal [13]. However, there are no reports of the application of SS as a support material for nanoparticle systems. There are many types of porous materials with different structural, textural, and morphological characteristics: the pore shape and size distribution, amount and type of surface functional groups, and others.

The characteristics of the material and the method of synthesis influence the deposition of nanoparticles on a material. During reduction, the first stage is the transfer of metallic ions from the bulk to the material, and the second stage is the reduction of the ions by a reducing agent. Therefore, the affinity of the support for the metal ions is crucial, although there is little information about this topic in the literature. In this sense, it is necessary to study and analyze how to properly select both the support and the type of nanoparticles that make up a composite.

Fluoride pollution in drinking water is a critical problem for human health in many countries, such as China, India, and Mexico. A high concentration of fluoride can cause fluorosis and neurological damage in humans. Therefore, researchers are focused on new, efficient methods to remove fluoride from water, and adsorption has been shown to be an effective and low-cost alternative [14]. Metal oxides have been reported as effective adsorbent materials for fluoride removal. Sadegh et al. [15] determined that nanomaterials have a high adsorption capacity due to their surface characteristics. Some researchers have combined different supports with Fe, La, Al, Mg, Zr, and bimetallic Al-Cu oxide nanoparticles [16]; however, this last material has not yet been applied in fluoride removal, and the method of synthesis used previously is different from that applied in the present work.

In this paper, the efficiency of black and white steel slag waste as a support material for Al/Cu oxide nanoparticles in the production of potential nanocomposites for fluoride removal from aqueous solution was studied. The nanocomposites were characterized by scanning electron microscopy (SEM), energy-dispersive X-ray spectroscopy (EDS), transmission electron microscopy (TEM), X-ray diffraction (XRD), and X-ray photoelectron scanning (XPS). Additionally, the pH at the potential of zero point charge (pH_{zpc}) and Brunauer–Emmett–Teller (BET) surface area were determined. In addition, kinetic experiments in a batch adsorption system were studied, and adsorber design was analyzed on a larger scale. Although the main idea was the study of nanocomposite behavior without constraining the pH, the effect of pH on adsorption was also studied in this research.

2. Materials and methods

2.1. Materials

Steel slags (SSs) were obtained from electric arc furnaces at the San Luis Potosí and Toluca stainless steel factories, México (SSLP and SST, respectively). The slags were treated as reported by Blanco-Flores et al. [17] for use in the synthesis of nanocomposites.

2.2. Method of preparation of nanocomposites

The reactor used for the synthesis was designed in such a way that the engineering parameters, such as the geometry of the reactor and the agitator, did not negatively affect the process. The dimensions of the tank were 11 cm in diameter and 13 cm in liquid height. A three-bladed propeller stirrer without baffles was used. The diameter of the stirrer was 4 cm.

The nanocomposites were synthesized using a chemical method reported by Blanco-Flores et al. [17] in a study to obtain an SSLP/Al–Cu nanocomposite composed of SSLP and Al–Cu nanoparticles. The other nanocomposite synthesized (SST/Al–Cu) was composed of SST and the same system of nanoparticles as that used in the previously reported method.

2.3. Characterization

SSLP, SST, SSLP/Al–Cu, and SST/Al–Cu were characterized by SEM using a JEOL JSM-6610LV SEM microscope to analyze the surface morphology coupled with an EDS source.

TEM images were obtained using a JEOL 1230 microscope operated at a 100 kV accelerating voltage. For TEM observations, the nanocomposite was dispersed in 2-propanol.

The phases of the SS were the most important factor affecting the deposition of the Al–Cu nanoparticles. Therefore, the main phases of the materials were decisive for the deposition of nanoparticles on SS waste. For this purpose, XRD was used to investigate the phase composition of SSLP, SST, SSLP/Al–Cu, and SST/Al–Cu. XRD analysis was performed with a Bruker D8 Advance X-ray diffractometer equipped with a CuK radiation source and SOL-X solid-state detector.

The chemical composition was analyzed by atomic absorption with a PerkinElmer 3110 spectrophotometer. The elemental concentrations of Al and Cu were determined with detection limits of 1.1 and 0.7 ppm, respectively. The pH_{zpc} of wastes and nanocomposites was determined by applying the method reported by Blanco-Flores et al. [18] using a Thermo Scientific Orion Star A325 pH meter.

The total surface area and pore size distribution were determined by N_2 adsorption–desorption isotherm using the BET method with a Micromeritics ASAP 2020 surface area analyzer and V4.01J software.

Wide and narrow XPS spectra were acquired using a JEOL JPS-9200 equipped with a Mg X-ray source (1,253.6 eV) at 200 W; the area of analysis was 3 mm², the pass energy (CAE) was 15 eV, and the vacuum was on the order of 7.5×10^{-9} Torr for all samples. The spectra were analyzed using the SpecsurfTM software included with the instrument, and all spectra were charge-corrected by means of the adventitious carbon signal (C1s) at 284.5 eV. The Shirley method was used for background subtraction, whereas for curve fitting, the Gauss–Lorentz method was used.

2.4. Adsorption kinetic experiments

The adsorption kinetics of fluoride were studied by using 400 mL of 3 mg L^{-1} fluoride solution with 2 g of SSLP/Al–Cu and SST/Al–Cu nanocomposites, which gave a ratio of 5 g composite L^{-1} solution. The mixtures were shaken for different times, and the adsorbent was separated from the liquid phase by decantation.

The effect of pH on the nanocomposites was examined. These experiments were carried out under the same experimental conditions as those mentioned above. The pH of the solution was fixed at 2, 4, 6, 8, 10, or 12. The mixture was shaken until the system reached equilibrium, and the adsorbent was separated by decantation.

All experiments were performed in duplicate at room temperature.

2.5. Adsorption experiments

A nanocomposite concentration of 5 g L^{-1} was placed in contact with different initial concentrations of fluoride (1–30 mg L^{-1}) and stirred until reaching equilibrium at room temperature. The mixtures were separated to determine the non-adsorbed fluoride content. The experiments were performed in duplicate.

To determine the effectiveness of the nanocomposites, experiments with SSLP and SST were performed under the same experimental conditions as mentioned above.

The fluoride concentrations in the solutions were measured with an ISE301F-specific ion electrode by using a total ionic strength adjustment buffer solution to eliminate interference from complexing ions.

The pH of the solutions was measured before and after treatment. The kinetics and adsorption data for the amount of fluoride adsorbed at a given time (q, mg g^{-1}) were calculated with Eq. (1).

$$q = \frac{C_i - C_t}{m} \times V \tag{1}$$

where C_i is the initial fluoride concentration (mg L^{-1}), C_t is the fluoride concentration in the solution (mg L^{-1}) at time t (min), V is the volume of treated solution (L), and m is the mass of the nanocomposite (g).

2.6. Batch adsorption: simple stage, cross-flow and counterflow approaches for determining the best nanocomposite for fluoride removal

Adsorption isotherms can be used to predict the design of simple-stage, cross-flow and counterflow batch adsorption systems. Therefore, it is possible to predict the behavior of adsorbers by using the best-fit equation of an adsorption isotherm model [19].

For the design, an initial fluoride concentration of 20 mg L^{-1}, a solution volume of 50 L, and 90% removal were established. A mass balance was performed to obtain the amount of material needed to reach the equilibrium concentration of fluoride (C_e, mg L^{-1}). For this calculation, Eq. (2) was used to model each adsorber design as the system parameters changed from q_0 (mg g^{-1}) to q_e (mg g^{-1}) and from $C_0 = 5$ mg L^{-1} to C_e, starting at time $t = 0$ (min) and $q_0 = 0$.

$$V \times (C_0 - C_e) = m \times (q_e - q_0)$$
$$V \times (C_0 - C_e) = m \times q_e \tag{2}$$

where q_0 and q_e (mg g^{-1}) are the amounts of fluoride adsorbed at the initial and equilibrium stages, respectively, and m (g) is the amount of nanocomposite added during the adsorption process. Eq. (2) allows the m value needed to treat 50 L of fluoride solution to be calculated for each design.

3. Results and discussion

3.1. Synthesis of SSLP/Al–Cu and SST/Al–Cu nanocomposites

The method of synthesis was chemical reduction based on the standard electrode potentials of Al^{3+}, Cu^{2+}, and BH$_4^-$ (−1.66, 0.34, and −1.24 V/SHE, respectively). As the Al–Cu nanoparticles were exposed to an aerobic atmosphere, they became mainly Al and Cu oxide nanoparticles. The formation of Al–Cu was achieved when these nanoparticles were adsorbed on the SS surface. Nanoparticle deposition occurred in the pores of the SS wastes. However, the differences between the surface characteristics for both solid wastes should affect the deposition of nanoparticles, as well as the properties of the final nanocomposites and the nanocomposite potential for use in environmental applications.

3.2. SEM analysis

To compare and understand the morphological characteristics of the nanocomposites, it was necessary to

analyze the surface of the SSLP and SST supports (Figs. 1a–d). Figs. 1a and d show overlapping dendritic phases. This trait is due to the different rates and solidification conditions of each component in the steel slag [20].

The SSLP micrographs showed a rough surface formed by dendritic layers of solidified material. Different wide circular spaces could be seen, but these spaces were not regarded as pore structures. The smooth surface of the particles was
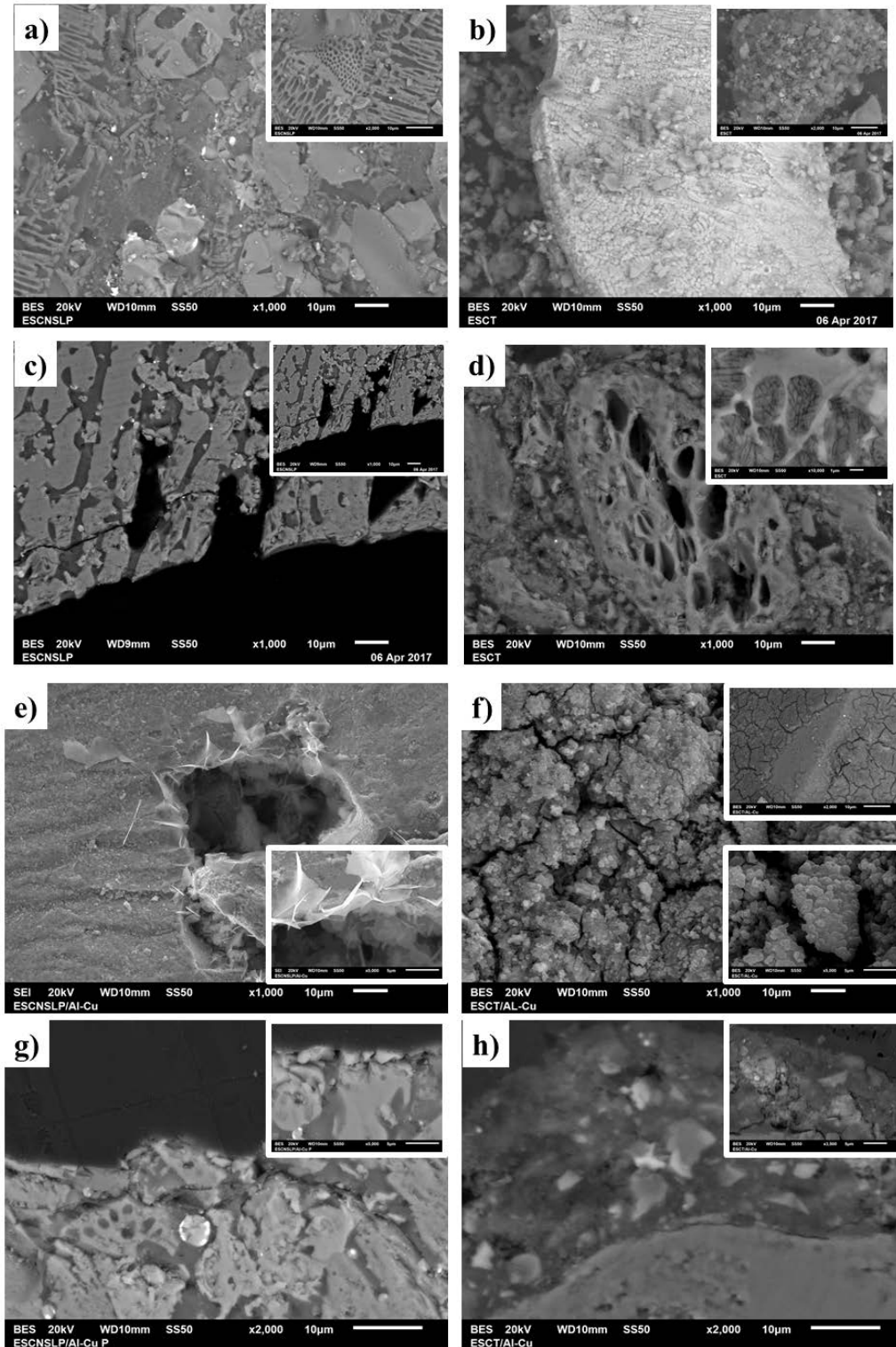
Fig. 1. SEM micrographs of SSLP ((a) and (c)) and SST ((b) and (d)) solid wastes and SSLP/Al–Cu ((e) and (g)) and SST/Al–Cu ((f) and (h)) nanocomposites. SEI, BES 20 kV, x1,000, x2,000, and x10,000.

due to the limited development of pores and the absence of aggregated nanoparticles (Figs. 1a–c). In Fig. 1c, open dendrites can be observed. These dendrites are accessible to the components of the liquid medium. SST had a different surface than SSLP. First, aggregated particles could be observed (Fig. 1b). Layers of solidified material and larger channels were observed. The dendrite structure was more compact and less elongated in SST. The channel structure was deformed and was more spheroidal than circular (Fig. 1d). Most likely, the porous structure was more developed in SST than in SSLP (Figs. 1c and d).

The surfaces of SSLP/Al–Cu and SST/Al–Cu (Figs. 1e and f) were less rough than the surfaces of SSLP and SST (Figs. 1a and b). The morphology seemed to be very different. The SSLP/Al–Cu surface was smoother than that of SST/Al–Cu. On the edges of the SSLP/Al–Cu channels, a new surface texture appeared; this texture could be attributed to Al–Cu deposition (Fig. 1e).

When this nanocomposite was fixed on epoxy resin (Fig. 1g), no major changes were visible on the surface of the SSLP due to the small amount of Al–Cu species or because these species were deposited on less-accessible sites on the material surface.

In Fig. 1f, a rough and cracked surface can be seen where Al–Cu species were supported on the SST. In contrast to SSLP/Al–Cu, there were many spheroidal particles on the surface of SST/Al–Cu. Therefore, it is possible that the morphology of the Al–Cu nanoparticles changed in each composite (Figs. 1e and f). The SST/Al–Cu fixed on epoxy resin (Fig. 1h) showed the formation of an outer layer surrounding the particles.

EDS demonstrated that the main phases in SSLP were composed of Fe, Si, O, and Ca, which formed calcium silicate, iron oxide, and other combinations, such as alloys and spinels, between the chemical elements S, Zn, Al, and Ti (Fig. 2a). The main phases of SST were metallic iron, iron oxide, calcium silicate, and others, such as iron, calcium, and aluminum compounds (Fig. 2b).

The information obtained from Fig. 1h was confirmed in Figs. 3a–c. Chemical mapping revealed the distribution of Al and Cu (Fig. 3b). The species of Al were fixed around the calcium–silicate phase of Ca in SST, and the species of Cu were distributed over the surface of the SST. Therefore, in contrast to Cu species, Al species showed more affinity for calcium phases. EDS (Fig. 3d) indicated that the outer layers were composed mainly of Al and Cu species. The texture of this new phase was different from the texture of the SST outer layer (Figs. 2b and 3c).

3.3. TEM analysis

On SSLP, the supported Al–Cu nanoparticles had tubular, trigonal, and spheroidal shapes (Figs. 4a and b). These shapes were related to the structure of SSLP because it has different shapes and cavities of various sizes (Figs. 1a and c). The tubular and spheroidal nanoparticles formed aggregates, probably because SSLP is a black steel slag with ferric phases that could promote the aggregation of particles.

TEM images confirmed the formation of spheroidal Al–Cu nanoparticles on SST (Figs. 4c and d). The structure of the support material determined the spherical shape of the

Al–Cu nanoparticles and their tendency to aggregate. This behavior matched the surface morphology of SST and may compromise fluoride removal.

The sizes of the supported Al–Cu nanoparticles on SSLP and SST are illustrated in Figs. 4e and f. The nanoparticles on SSLP were larger than those on SST. This result again confirmed the influence of the support material on the size and shape of nanoparticles.

3.4. XPS analysis

XPS analysis allowed the identification of the interaction between Al–Cu nanoparticles and elements in the support material and their chemical environment and oxidation state. Figs. 5a–c show the XPS spectra for the SSLP/Al–Cu nanocomposite. The Al 2p spectrum (Fig. 5a) has four peaks: 72.4, 74.2, 75.3, and 76.4 eV, which were referenced and identified as the alloy, spinel, oxide, and hydroxide of aluminum, respectively. In this case, Al retained its oxidation state of 3+ [21]. The formation of Al–Cu alloy, Cu^{2+}–O, and Al–Cu–O spinel [22] and the interaction among Si, Al, O, and Cu can be distinguished [23] in the Cu $2p_{3/2}$ lines in the XPS spectrum (Fig. 5b). The presence of the aforementioned chemical species was confirmed from the combined results of the O 1s lines (Fig. 5c).

In the case of the SST/Al–Cu nanocomposite, the four peaks for Al 2p at 72.1, 73.5, 75.4, and 76.7 eV were assigned to Al–Cu alloy, Al–Cu–O spinel, and the oxide and hydroxide of aluminum, respectively [24,25] (Fig. 5d). The spectrum of Cu $2p_{3/2}$ shows five peaks (Fig. 5e). The peaks at 933.6 and 934.4 eV were related to Cu^{2+} species, but there was no Cu^+ because the signal below 932 eV was absent. The peak at 936.1 eV was attributed to the Si(Al)–O–Cu interaction in which Cu^{2+} is coordinatively unsaturated [26]. This signal could be consistent with some elements of SST phases. The presence of Al–Cu–O spinels was consistent with the peak at 935.7 eV [26]. The Al–Cu alloy was confirmed by the peak at 933.3 eV. Seo et al. [24] also reported this signal. The O 1s spectrum was deconvoluted into five peaks (Fig. 5f) for AlOOH, CuO, CaO, Si–O, and H_2O compounds, which confirmed the results obtained from the Al and Cu XPS spectra and SEM–EDS [21].

Therefore, the species of Al–Cu nanoparticles formed during synthesis were the same for both materials, despite the fact that the materials have different physicochemical characteristics. Interactions were established between –O, –OH, Si–O, Ca–O, and Al–Cu. These compounds appeared because silicates and calcium ions are present in the main phases of SSLP and SST. Interactions between Fe and oxidized materials were not observed because the nanoparticles are not associated with ferric phases. This behavior has been reported in previous studies in which Fe–Cu nanoparticles were applied for dye removal [27]. The characteristics of the support material and the distribution of Al–Cu nanoparticles are the most critical factors for fluoride removal. Therefore, the experimental conditions during synthesis are responsible for the formation of the same species of Al–Cu nanoparticles on both materials.

3.5. XRD analysis

The Al–Cu nanoparticles that were obtained in the solution after synthesis were isolated to analyze the Al and
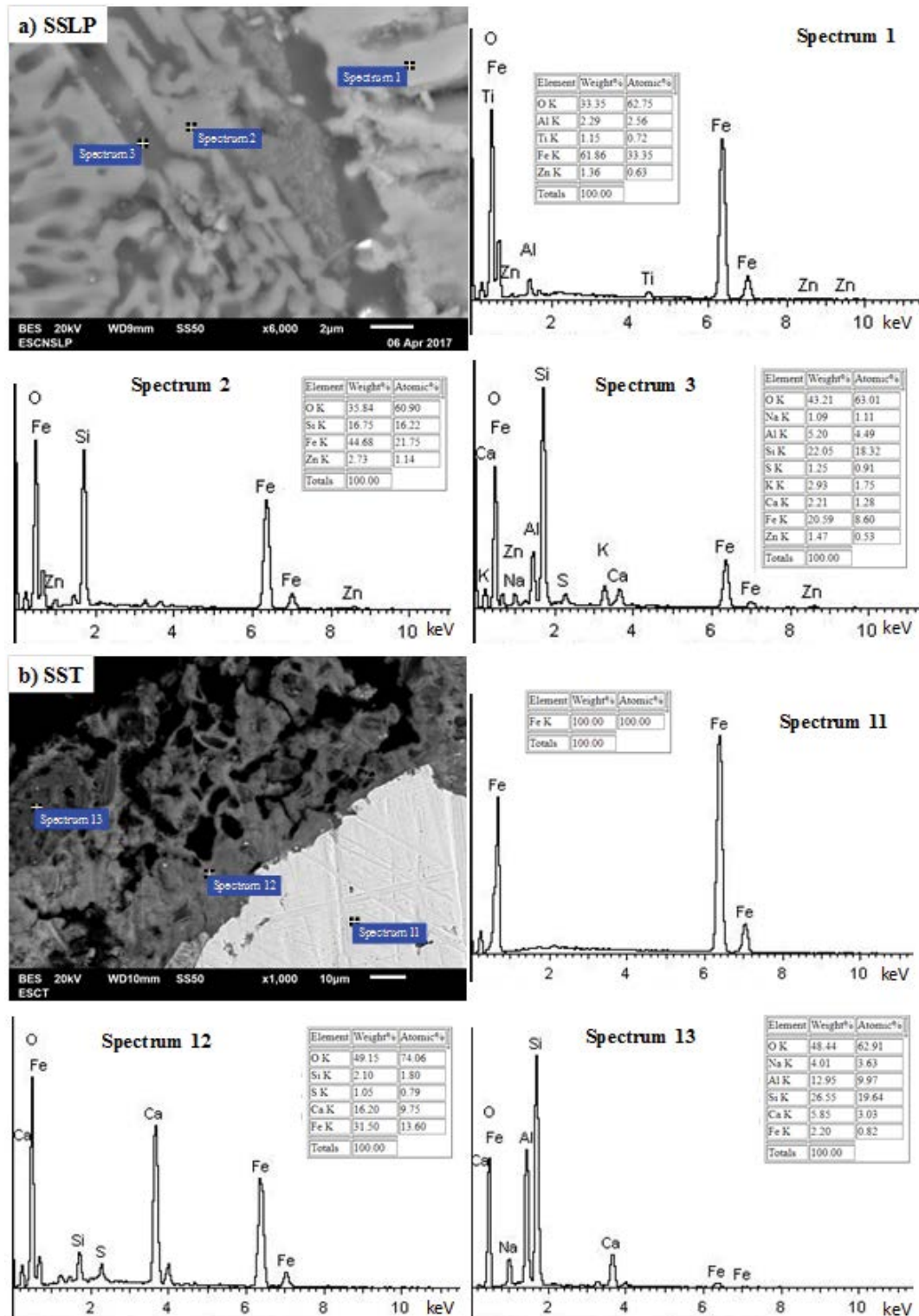
Fig. 2. SEM–EDS analysis of SSLP and SST solid waste.

Cu species by XRD. The nanoparticles were oxides and alloys of Al and Cu (Fig. 6a). Because Cu nanoparticles are very reactive, some species were oxidized to 1+; this was mainly due to the absence of a capping agent to prevent the oxidation process [28].

The nanoparticles supported on SSLP and SST were Al and Cu oxides, alloys, spinels, and aluminum hydroxide (Figs. 6c and e). In both nanocomposites, the Cu species achieved an oxidation state of 2+. Therefore, the formation of Al–Cu nanoparticles may be influenced by the chemical
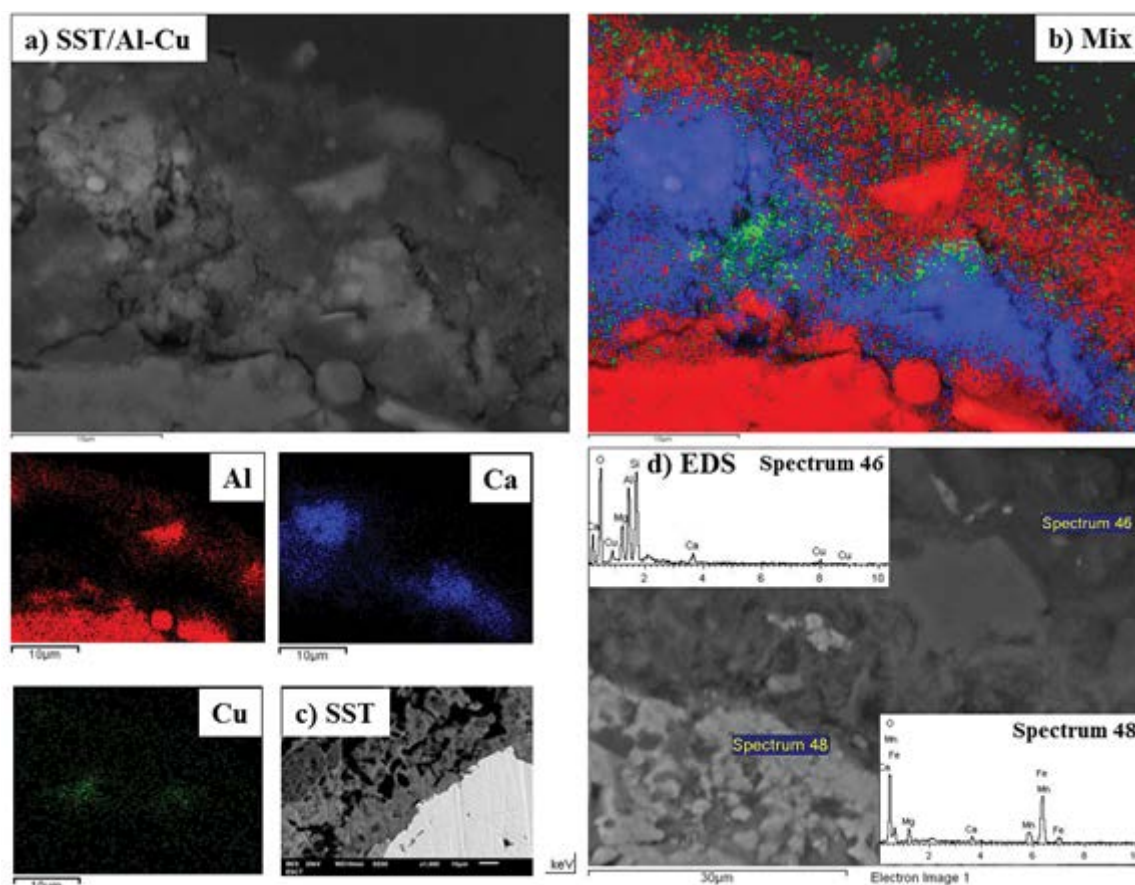
Fig. 3. Chemical mapping and EDS analysis of the SST/Al–Cu nanocomposite.

reduction method used instead of the chemical phases present in SSLP and SST (Figs. 6b and d).

The phases of the SST and SSLP waste matched the chemical elements determined by atomic absorption and EDS techniques (Fe, Cu, Ca, and Si).

3.6. Chemical composition and pH$_{zpc}$ of nanocomposites

The chemical composition of the solid wastes suggested that the main elements present in both wastes were Fe and Ca. SSLP is a steel slag enriched with iron, and SST is a steel slag enriched with calcium. In addition, Cu is prevalent at a higher proportion in SSLP than SST waste. In both nanocomposites, after synthesis, the amounts of Fe and Ca decreased from the initial values, and the amount of Cu increased (Table 1).

For SSLP/Al–Cu and SST/Al–Cu, the ratio between Al and Cu was 0.39 and 4.54, respectively. According to the Al/Cu ratio, the amount of Al is higher than that of Cu in SST. This may be related to the content of Fe and Ca phases. When the support contains more Fe phases, which is the case for SSLP, Cu deposition increases, but when the material presents a greater quantity of Ca (SST), Al deposition is favored. Therefore, for these supports, the affinity of nanoparticle deposition depended on the main element in the chemical composition of the support. Therefore, the physicochemical properties of SSLP and SST waste promote the deposition of Al–Cu nanoparticles at different proportions.

The pH$_{zpc}$ of SSLP/Al–Cu was smaller than the pH$_{zpc}$ of SST/Al–Cu (6.09 and 8.54, respectively). Therefore, the distribution of charge on internal and external surfaces was higher for SST than for SSLP. The difference between the pH$_{zpc}$ values of SSLP (5.99), SST (9.35), SSLP/Al–Cu, and SST/Al–Cu indicated that the surface of the solid waste was modified when Al–Cu nanoparticles were deposited. SST desorbed ions, which led to the decrease in pH$_{zpc}$. These ions may be Ca^{2+} because SST is richer in calcium (16.74%) than is SSLP (1.44%), according to the chemical composition obtained by atomic absorption.

3.7. Surface area analysis

Adsorption–desorption isotherms were obtained at 77 K for SSLP/Al–Cu and SST/Al–Cu (Figs. 7a and b) by BET analysis. According to the results, the samples were classified as mesoporous–macroporous materials. As the adsorption and desorption branches were similar, the nanocomposites were slightly heterogeneous in their porous structure. In terms of IUPAC classification [29], the hysteresis curves were classified as H4, which characterizes solids formed by aggregates of particles with pores of uniform size or shape. These results corroborate the results obtained from SEM analysis.

The specific area of SST/Al–Cu (4.17 m^2 g^{-1}) was seven times larger than the specific area of SSLP/Al–Cu (0.58 m^2 g^{-1}). These values were lower than other values reported in the literature for other adsorbent materials [8,30].
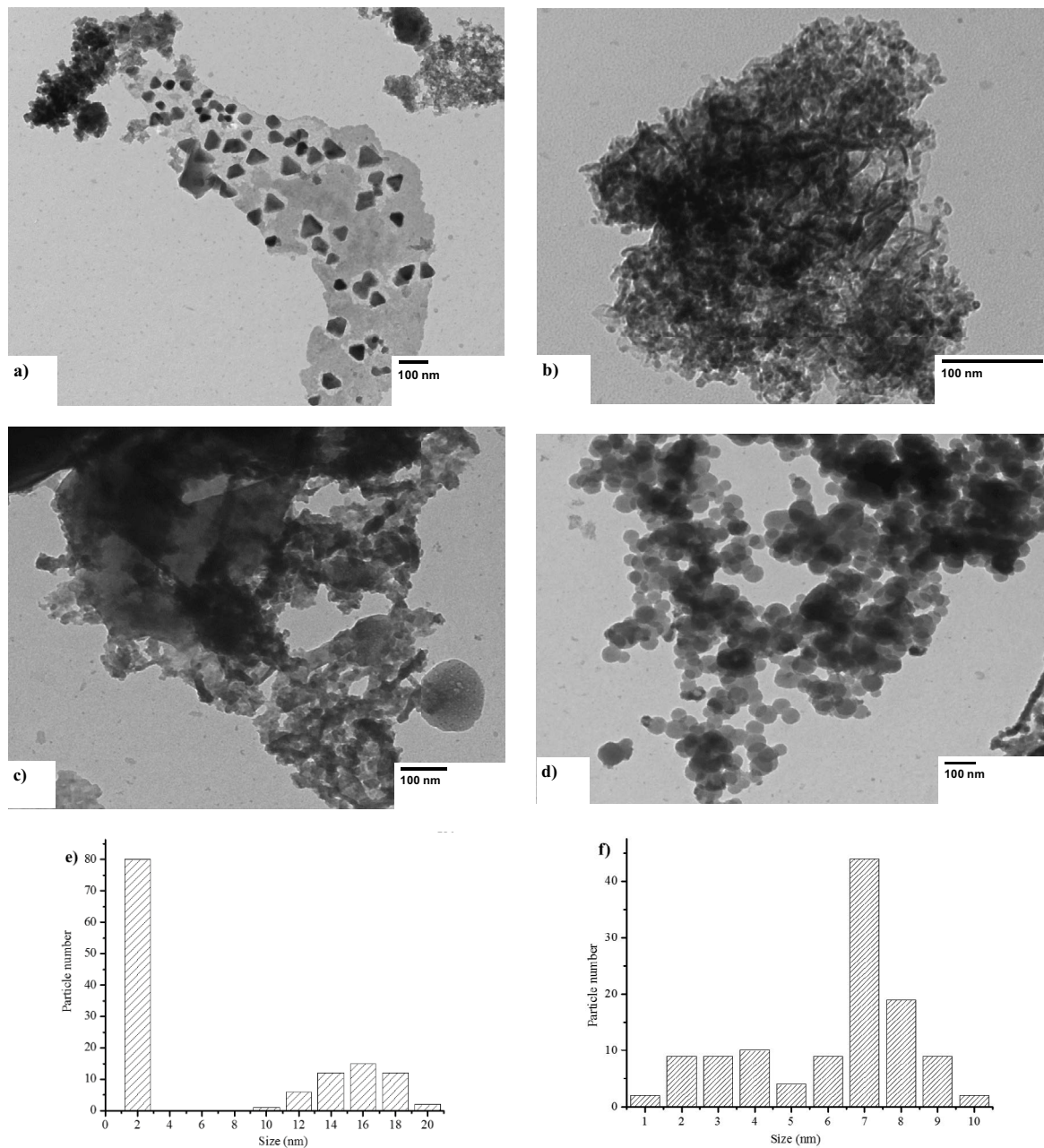
Fig. 4. TEM images of the SSLP/Al–Cu ((a) and (b)) and SST/Al–Cu ((c) and (d)) nanocomposites. Histogram of synthesized Al–Cu nanoparticles supported on SSLP (e) and SST (f) waste.

3.8. Kinetic adsorption experiments

The adsorption rate depends on the affinity between the adsorbent and adsorbate and their characteristics. Kinetic experiments were performed for the four materials. The highest adsorbed amount was achieved in the first 100 min (Fig. 8a). The equilibrium time (t_e) increased in the order of SSLP < SST < SST/Al–Cu < SSLP/Al–Cu (Table 2). The equilibrium time may have increased for the composites with respect to SST and SSLP because the adsorption sites might be less accessible due to agglomeration of nanoparticles on the surfaces. In addition, the differences among

the equilibrium times are related to the different adsorption mechanisms and the textural, morphological, and structural characteristics of the materials.

After adsorption, all solutions were analyzed to determine whether the nanoparticles would desorb from the material. According to the results, the SSLP/Al–Cu material did not desorb Al. In contrast, the SST/Al–Cu composite desorbed a concentration of 5.34 mg L^{-1}. The Cu concentrations were 0.09 and 0.17 mg L^{-1} from SSLP/Al–Cu and SST/Al–Cu, respectively. According to the maximum permissible limits for nondomestic wastewater discharges in Mexico, the maximum concentrations of Al and Cu are 10 and 3 mg L^{-1}, respectively.
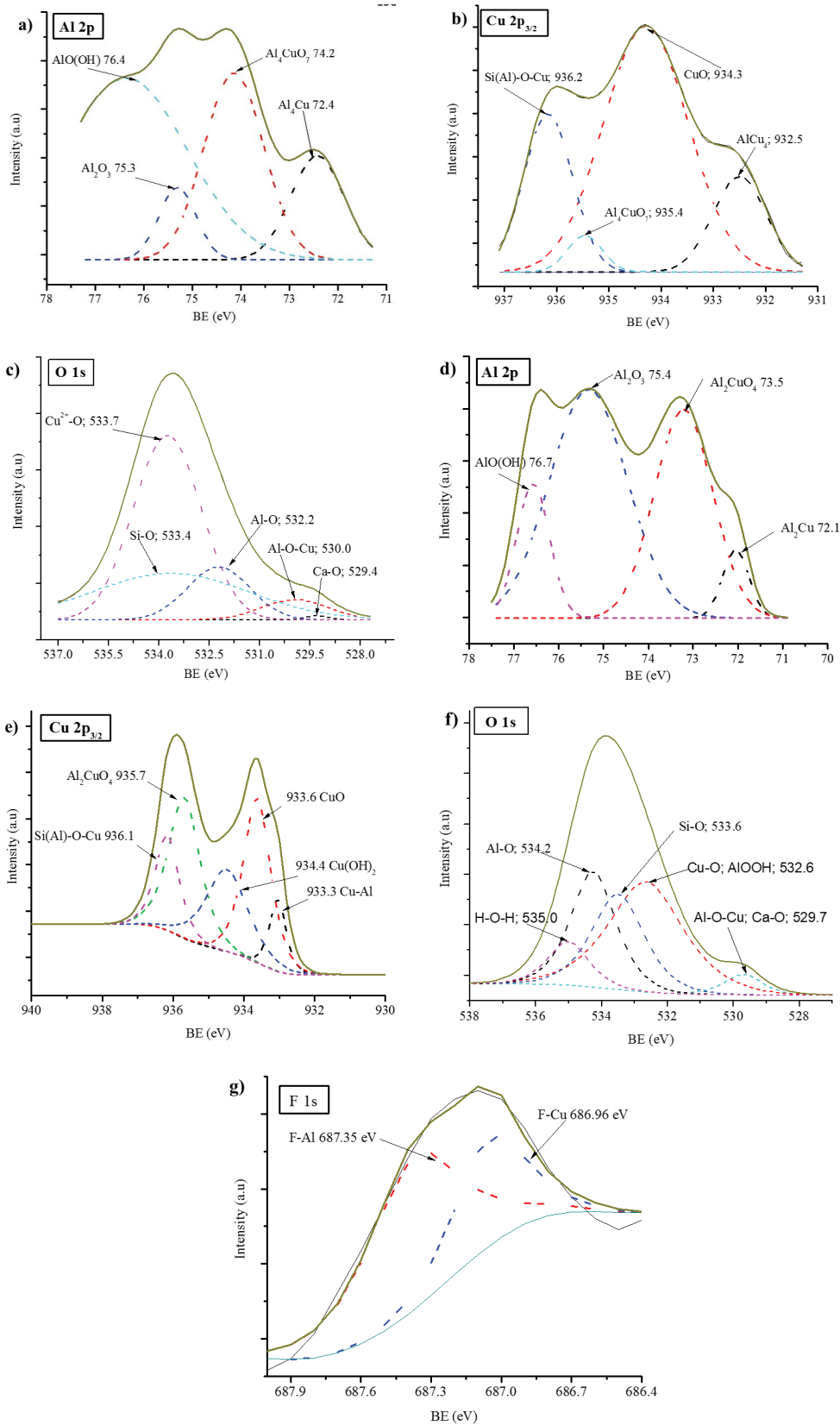
Fig. 5. Narrow-scan XPS spectra of Al 2p, Cu 2p$_{3/2}$, and O 1s deconvolution from SSLP/Al–Cu ((a) and (c)), SST/Al–Cu ((d) and (f)) nanocomposites, and the interactions between F–Cu and Al–F (g).
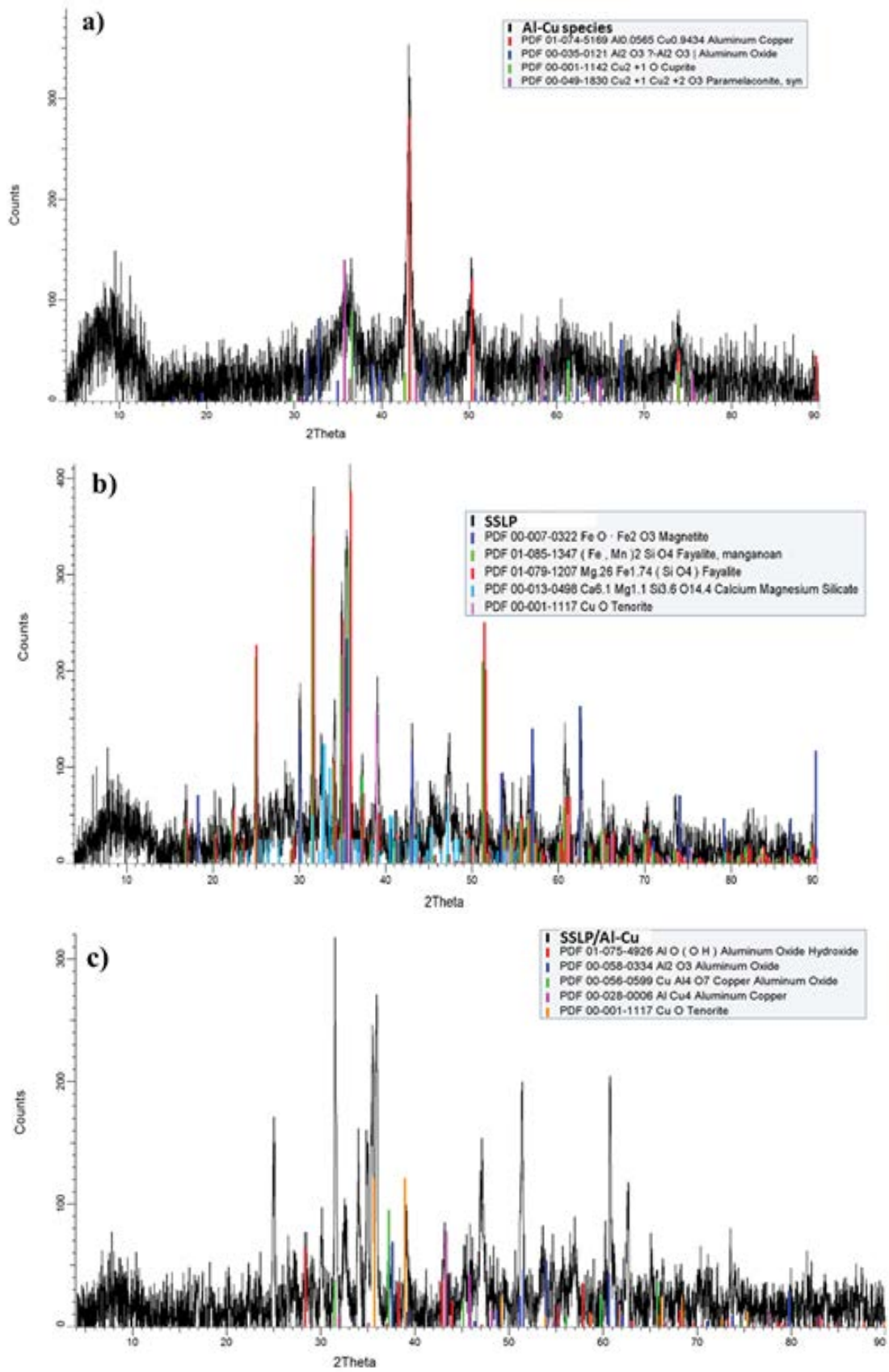
(Fig. 6 continued)
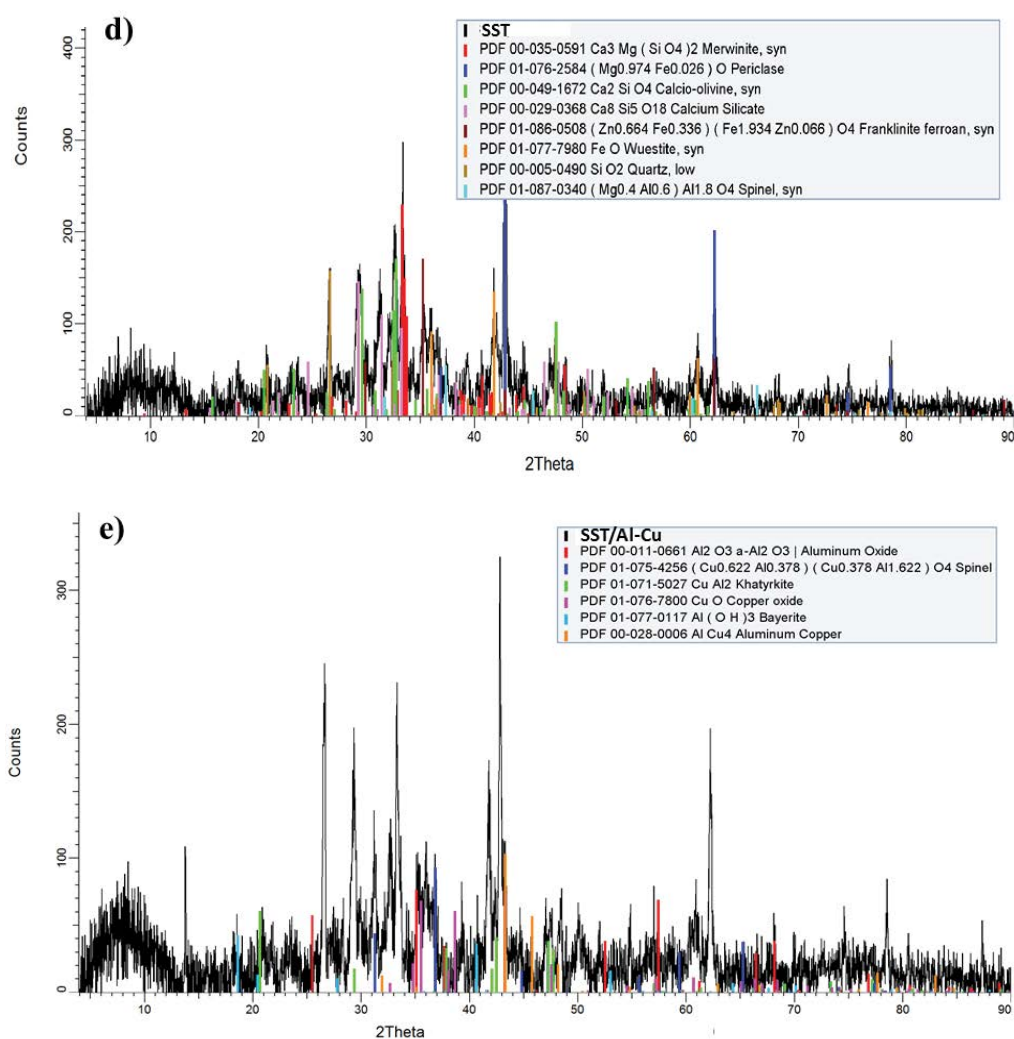
Fig. 6. X-ray diffraction patterns of Al–Cu nanoparticles (a), SSLP (b), SSLP/Al–Cu (c), SST (d), and SST/Al–Cu (e).

Therefore, the nanocomposites were feasible for use in this application.

Pseudo-first-order, pseudo-second-order, and second-order models [31,32] were applied to the experimental data in all cases. The obtained kinetic parameters (Table 2) were used to identify the model of best fit.

A combination of the pseudo-second-order and second-order models best described the adsorption process in the case of SST and SSLP. The pseudo-first-order model better described the process for SST/Al–Cu, although the statistical parameters also confirmed a good fit with the pseudo-second-order model. Therefore, chemisorption may have occurred through the sharing of electrons by valence forces between the adsorbate and Al–Cu oxide nanoparticles supported on the waste surfaces; nevertheless, physisorption could also occur. The adsorption kinetics on SSLP/Al–Cu took place by a chemisorption process since the best-fitted model was the pseudo-second-order model. Therefore, the supported Al–Cu nanoparticles on SSLP induced a similar adsorption behavior to that induced by SST/Al–Cu. In the case of SST, the deposition of Al–Cu nanoparticles was

affected by the mechanism by which the fluoride ions were adsorbed on the nanocomposite surface because the Al and Cu nanoparticles could interact through surface vacancies, free electrons, and fluoride ions [26].

The intraparticle diffusion model [33] was applied for all materials (Table 3). In all cases, multilinear plots were

Table 1
Chemical composition of SSLP, SST, SSLP/Al–Cu, and SST/Al–Cu materials

Materials	Percentage chemical composition (%)			
	Al	Cu	Fe	Ca
SSLP	–	11.9	39.9	1.44
SST	–	0.17	13.36	16.74
SSLP/Al–Cu	4.74	12.16	35.12	1.00
SST/Al–Cu	6.90	1.52	10.96	16.6
Al–Cu Nps	8.51	7.64	–	–
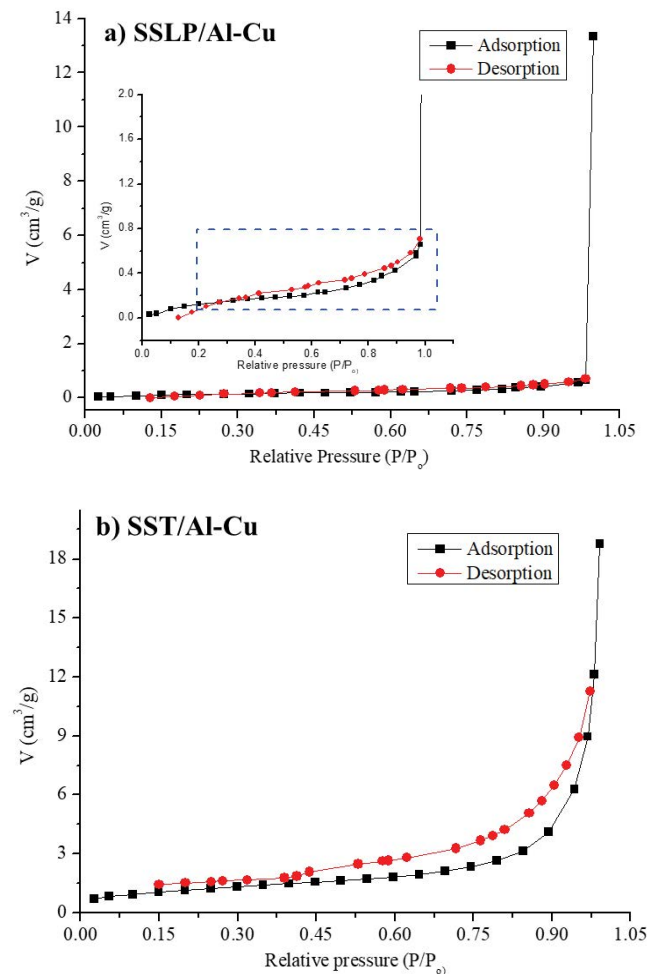
Fig. 7. N$_2$ adsorption–desorption isotherms of SSLP/Al–Cu (a) and SST/Al–Cu (b) nanocomposites.

Fig. 8. Kinetic adsorption of SSLP, SST, SSLP/Al–Cu, and SST/Al–Cu materials (a) and study of the effect of pH on nanocomposites (b).

observed. Since the plots did not pass through the origin, intraparticle diffusion was not the only rate-controlling step. After 80 min, SST showed a process of desorption, and therefore, only two linear zones appeared in the plot. The *C* constant increased in the order SST < SSLP < SSLP/Al–Cu < SST/Al–Cu. This behavior indicates that superficial adsorption on the SST/Al–Cu material had a major contribution during the process because this variable (*C*) represents the boundary layer effect. This statement is also related to the lower k_i (intraparticle rate constant) value and the equilibrium time. Most likely, the aggregation of nanoparticles made the surface rougher and the diffusion process more difficult. Additionally, in SST, the Al–Cu nanoparticles were deposited around the SST particles, widening the boundary film. For the nanocomposites, the values of *C* were increased relative to the values obtained for SST and SSLP.

As *C* was higher than k_i, the external transport was greater than the internal transport, and therefore, the Boyd model, representing the difference between intraparticle and film diffusion, was applied [34]. If the straight lines do not pass through the origin, then film diffusion is the rate-limiting step. Table 3 shows the k_i, *C*, and diffusivity of F$^-$ in the pores

(D_p) and the effective diffusion coefficient (D_i) [35]; these values were calculated from Eqs. (3) and (4).

$$k_i = \frac{12q_e}{d_p}\sqrt{\frac{D_p}{\pi}} \tag{3}$$

$$B = \frac{\pi^2}{r^2}D_i \tag{4}$$

where q_e is the adsorption capacity at equilibrium (mg g^{-1}), and D_p and *r* (cm) are the diameter and radius of the particles, respectively. *B* was obtained from the slope of the linear plot B_t vs. *t* [35].

When the nanoparticles were supported, the resistance to external mass transfer increased; for this reason, the D_p value decreased for the nanocomposites (Table 3). As the D_i values were on the order of 10^{-6}–10^{-5} cm^2 min^{-1}, intraparticle or pore diffusion was not the rate-limiting step in the adsorption process [23].

3.9. Effect of solution pH

As the pH of the fluoride solution increased, the adsorption capacity of the nanocomposites increased (Fig. 8b).

Table 2
Kinetic parameters of fluoride adsorption onto SSLP, SST, SSLP/Al–Cu, and SST/Al–Cu materials

Parameters	SST	SST/Al–Cu	SSLP	SSLP/Al–Cu
	t_e = 80 min	t_e = 130 min	t_e = 30 min	t_e = 380 min
	$q_{e,exp}$ = 0.086 mg g^{-1}	$q_{e,exp}$ = 0.195 mg g^{-1}	$q_{e,exp}$ = 0.065 mg g^{-1}	$q_{e,exp}$ = 0.099 mg g^{-1}
Pseudo-first-order model				
$q_{e,cal}$ (mg g^{-1})	0.082	0.199	0.064	0.11
k_1 (min^{-1})	0.11	0.15	0.47	1.37
R^2	0.9096	0.9336	0.9870	0.9019
RSS	0.00041	0.0024	0.00042	0.0011
X^2	0.00083	0.00024	0.00053	0.00015
Pseudo-second-order model				
$q_{e,cal}$ (mg g^{-1})	0.090	0.206	0.065	0.105
k_2 (g mg^{-1} min^{-1})	1.82	1.34	22.53	0.11
R^2	0.9621	0.9746	0.9927	0.9382
RSS	0.00017	0.00092	0.00003	0.00068
X^2	0.000035	0.000092	0.000003	0.00097
Second-order-model				
a (mg g^{-1} min^{-1})	0.069	69.94	17.38	0.19
b (mg g^{-1})	70.63	70.28	65.17	71.99
R^2	0.9816	0.9629	0.9952	0.7999
RSS	0.000084	0.0014	0.000024	0.0022
X^2	0.000017	0.00014	0.000003	0.00031

Table 3
Intraparticle diffusion parameters for SSLP, SSLP/Al–Cu, SST, and SST/Al–Cu materials

Material	k_i (mg g^{-1} min^{-1})	C	Linear zone	D_p (cm^2 min^{-1})	D_i (cm^2 min^{-1})
SSLP	0.0064	0.0648	3	7.44×10^{-7}	3.33×10^{-6}
SSLP/Al–Cu	0.00084	0.0936	3	5.61×10^{-9}	1.67×10^{-5}
SST	0.0022	0.0647	2	5.06×10^{-8}	6.05×10^{-6}
SST/Al–Cu	0.00058	0.1869	3	6.79×10^{-10}	6.06×10^{-6}

Higher removal was achieved at pH values between 4.4 and 7.7 for both nanocomposites. Although the curves of pH dependence were similar for the two adsorbents, the best response was obtained for the SST/Al–Cu nanocomposite. The F$^-$ adsorption at pH = 4 increased because the higher concentration of H$^+$ made the surface more positive and the attraction of fluoride ions increased. At basic pH values, the concentration of $^-$OH was higher, and the ions (F$^-$ and $^-$OH) competed for adsorption sites. Ma and Chen [36] reported a similar result, achieving a higher adsorption capacity at pH 4 and a lower capacity at pH 12.

3.10. Adsorption isotherm

Adsorption isotherms were obtained for all materials (Fig. 9). The concentration range was expanded, but all the isotherms had the same behavior. The results indicated that multilayer adsorption took place at low concentrations until saturation was reached. At low concentrations,

the adsorption capacity increased linearly. A plateau was obtained for all materials at higher initial concentrations under the selected experimental conditions. In contrast, the amount of F$^-$ adsorbed onto SST/Al–Cu and SSLP/Al–Cu was similar until the materials were saturated.

The Langmuir, Freundlich, Langmuir–Freundlich, Temkin, Redlich–Peterson, and Dubinin–Radushkevich adsorption isotherm models [37,38] were applied to the experimental data, and the parameters of these models were determined with their respective statistical variables (Table 4).

The Langmuir–Freundlich model achieved the best correlations for the isotherm data for SST, SST/Al–Cu, and SSLP/Al–Cu, and the Redlich–Peterson model achieved the best correlation for SSLP/Al–Cu. The Langmuir–Freundlich model assumes a combination of mechanisms: chemisorption and physisorption, among others. The Redlich–Peterson model shares features of the Langmuir and Freundlich isotherms but does not follow monolayer adsorption [39].
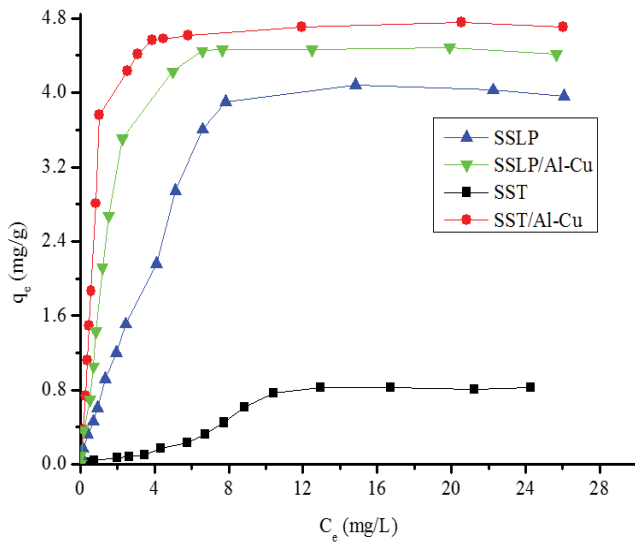
Fig. 9. Adsorption isotherms for SSLP, SSLP/Al–Cu, SST, and SST/Al–Cu.

The results obtained for the Langmuir–Freundlich constant (K_{LF}) indicated that the adsorption process for SST, SSLP, and SSLP/Al–Cu was characterized by multilayer adsorption because the K_{LF} values were lower than 1. This behavior was confirmed in the Langmuir model by the k_L constant, whose small values specified a weak interaction between the adsorbate and adsorbents [40].

The maximum adsorption capacity increased in the order SST < SSLP/Al–Cu ≈ SSLP < SST/Al–Cu. Therefore, the best material for fluoride removal was SST/Al–Cu, although its adsorption capacity was not very different from those of SSLP/Al–Cu and SSLP. In addition, the greatest affinity for fluoride ions was achieved by SST/Al–Cu, based on the Langmuir constant k_L and the shape of the adsorption isotherm at low concentrations. The $1/n$ value from the Freundlich model for all materials was between zero and one; therefore, the adsorption process was classified as favorable.

The Dubinin–Radushkevich model assumes multilayer adsorption on homogeneous and heterogeneous surfaces; this model may also distinguish between physical and chemical adsorption. The adsorption energy (E) values were

Table 4
Isotherm adsorption parameters of solid wastes and nanocomposites for fluoride adsorption

Parameters	SST	SST/Al–Cu	SSLP	SSLP/Al–Cu
Langmuir model				
q_m (mg g^{-1})	1.92	5.25	5.18	5.16
k_L (L g^{-1})	0.04	1.19	0.21	0.60
R^2	0.8909	0.9513	0.9588	0.9647
Freundlich model				
K_F (mg g^{-1})(L mg^{-1})$^{1/n}$	0.009	2.64	1.15	1.99
$1/n$	0.74	0.24	0.44	0.31
R^2	0.8589	0.7543	0.8723	0.8308
Langmuir–Freundlich model				
q_m (mg g^{-1})	0.86	4.68	4.30	4.26
K_{LF} (L mg^{-1})	5.78×10^{-4}	2.44	0.13	0.64
$1/n$	0.26	0.36	0.59	0.50
R^2	0.9776	0.9925	0.9813	0.9974
Temkin model				
a (L g^{-1})	1.02	16.17	4.66	11.06
B_T (J mol^{-1})	0.25	0.95	0.85	0.89
R^2	0.7747	0.8689	0.8714	0.8980
Redlich–Peterson model				
K_r	0.06	4.74	0.68	2.19
a_r (L g^{-1})	8.95×10^{-7}	0.64	0.01	0.21
b_r (L mg^{-1})	4.33	1.14	1.78	1.25
R^2	0.9382	0.9705	0.9924	0.9879
Dubinin–Radushkevich model				
DB	7.21×10^{-6}	1.32×10^{-7}	1.25×10^{-6}	3.10×10^{-7}
q_m (mg g^{-1})	0.95	4.75	4.03	4.52
E (kJ mol^{-1})	0.26	1.95	0.63	1.27
R^2	0.9638	0.9905	0.9576	0.9949

0.26 and 1.95 kJ mol⁻¹, which indicated that removal might occur through a physisorption process involving van der Waals forces that originate from the supported nanoparticles [41]. The best correlation for this model was achieved for the SST/Al–Cu and SSLP/Al–Cu nanocomposites.

Several researchers have developed synthetic materials based on oxide/hydroxide metals for fluoride removal. The authors reported that metal oxides, hydroxides, and oxyhydroxides facilitate the adsorption of anions such as F⁻ due to the positive and negative charges on the surface of the materials [42]. F⁻ adsorption took place at different pH values for each material (Table 5). For SST and SST/Al–Cu, pH_f was lower than pH_{zpc}, and therefore, adsorption was achieved by electrostatic attraction, ion exchange or complexation reactions on the solid surface. This process can be represented by the following mechanisms:

$$= Al - \left(OH\right)_3 + {}^-OH \rightarrow -AlOH_2^+ + F^- \rightarrow Al - F^- + H_2O$$
$$= Cu - \left(OH\right)_2 + F^- \rightarrow = Cu - F + H_2O \quad (5)$$
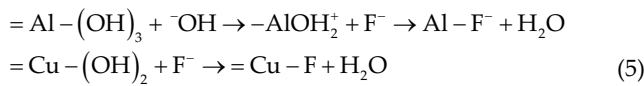
This process may have occurred because the synthesized Al/Cu nanoparticles were formed of oxide, hydroxide, and spinel phases, which exposed positive charges on the surface of the nanocomposite and improved the adsorption capacity. The interactions between F–Cu and Al–F were confirmed by the XPS results (Fig. 5g).

An opposite trend in pH parameters was observed for SSLP and SSLP/Al–Cu. This behavior was attributed to adsorption over a neutral and a negative solid surface for SSLP and SSLP/Al–Cu, respectively. In the process using SSLP, the pH_f was equal to the pH_{zpc}, and in the process using

Table 5
pH of the final solution and zero-point charge pH for SSLP, SSLP/Al–Cu, SST, and SST/Al–Cu

Parameter	SSLP	SSLP/Al–Cu	SST	SST/Al–Cu
pH_f	5.78–6.20	7.16–7.90	8.98–9.00	7.56–7.96
pH_{zpc}	5.99	6.09	9.35	8.54
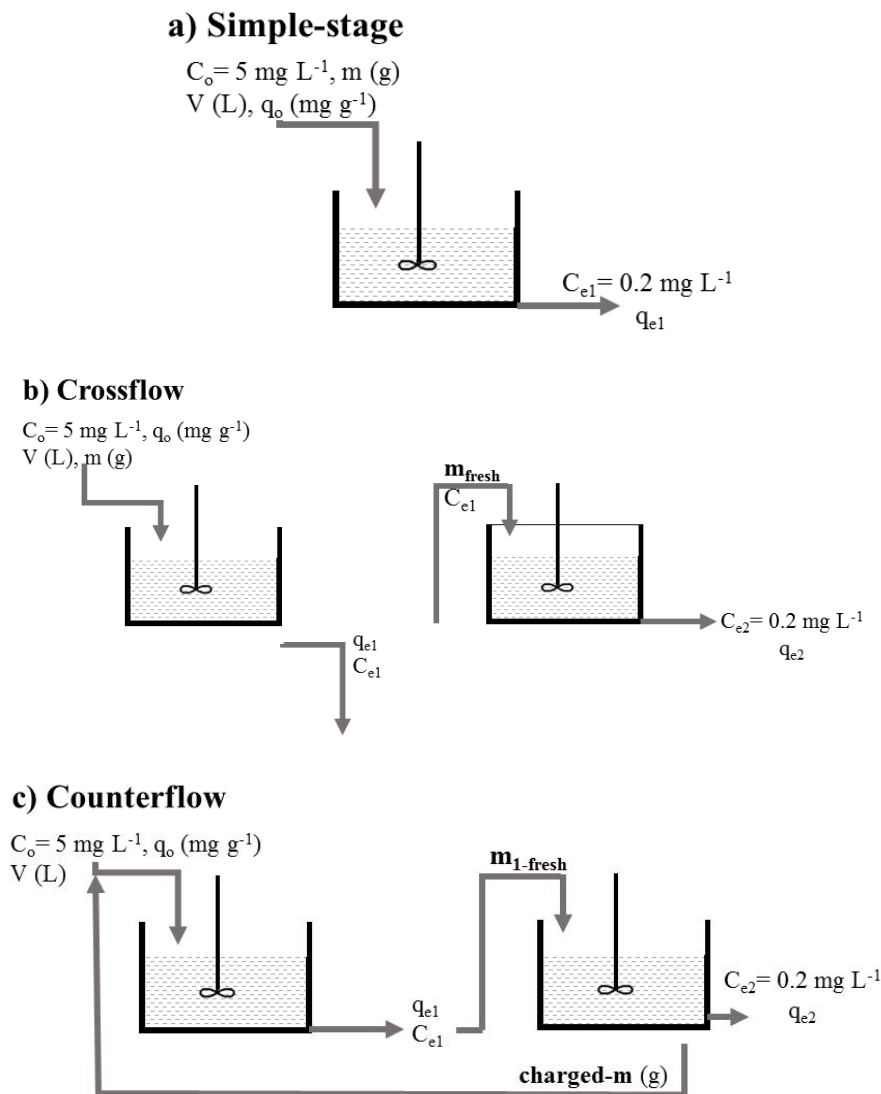
Fig. 10. Simple-stage, cross-flow, and counterflow batch adsorber design for fluoride adsorption on SST/Al–Cu nanocomposites.
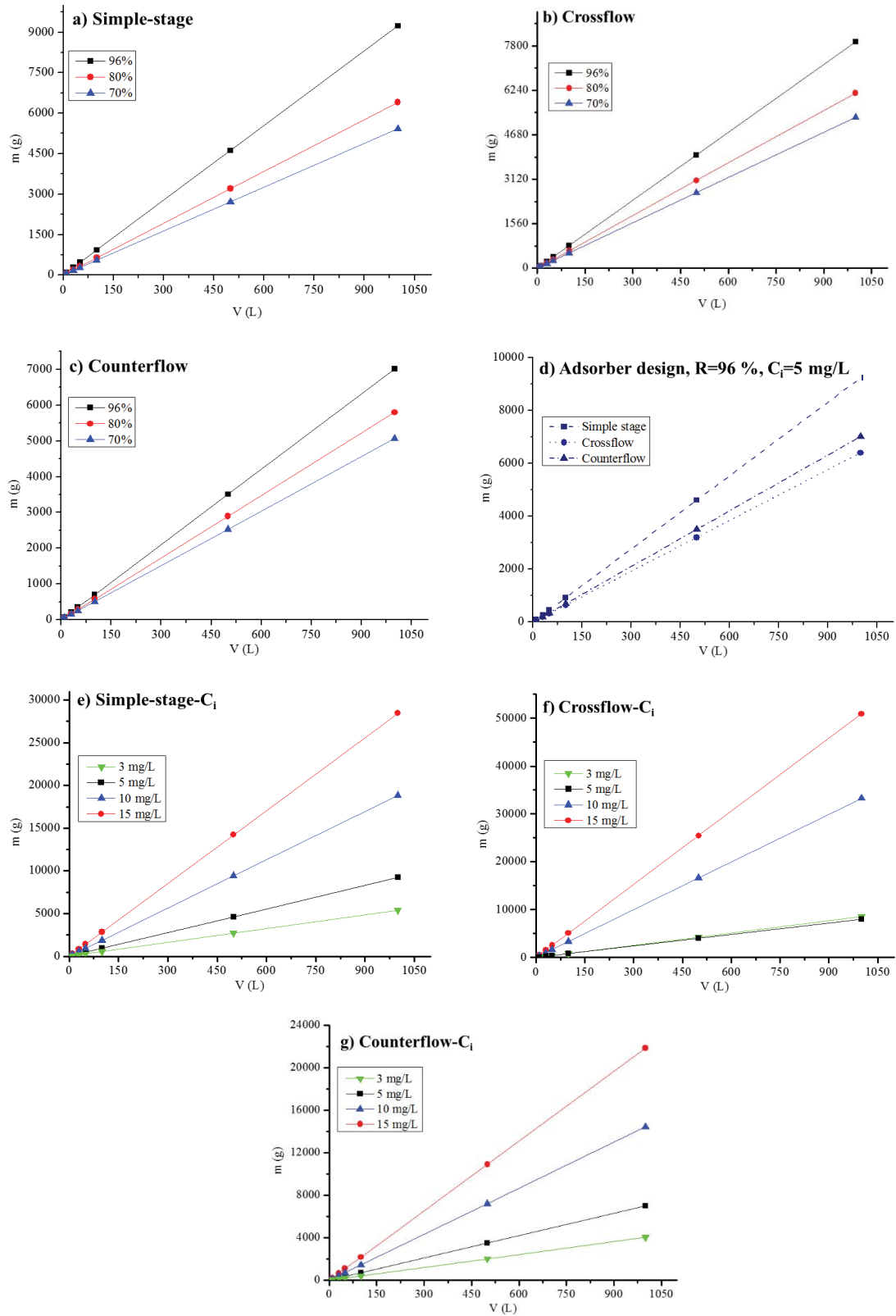
Fig. 11. Plots of *m* (g) of SST/Al–Cu required vs. volume (L) of F⁻ solution for simple-stage (a), cross-flow (b), and counterflow (c) batch adsorbers for different adsorption percentages (%R), C_0 = 5 mg L⁻¹. In addition, plots of *m* (g) of SST/Al–Cu required vs. volume (L) of F⁻ solution for simple-stage (e), cross-flow (f), and counterflow (g) batch adsorbers at different initial concentrations (mg L⁻¹) and 96% adsorption.

the SSLP/Al–Cu nanocomposite, the pH_f was higher than the pH_{zpc}; the repulsion force between F⁻ and surface groups also affected the results [43].

Although several authors have reported that the F⁻ adsorption process is more favorable at low pH values [44], in these cases, the adsorption behavior was different. SST achieved a pH higher than 7.00 when Al–Cu nanoparticles were supported on it, and the resulting material achieved the highest adsorption capacity. The final pH increased to slightly above 7.00 as F⁻ removal increased. Although the final pH of the solution with SSLP/Al–Cu was lower than that of the solution with SST/Al–Cu, the surface characteristics of the first nanocomposite did not favor F⁻ removal.

The Fe phases of SSLP were inactive and did not influence the removal process. In areas where Al–Cu nanoparticles were deposited (Figs. 3a and b), the adsorption process should be more positive and efficient because the fluoride ions may interact with the nanoparticles. Therefore, the larger amount of Al–Cu nanoparticles on SST than on SSLP made the former composite more efficient for F⁻ removal than SSLP/Al–Cu was.

3.11. Designing single-stage, cross-flow and counterflow batch adsorbers from equilibrium data

Design analysis is usually applied to predict the behavior of an adsorption system at various amounts of adsorbent, removal percentages, and wastewater volumes. F⁻ adsorption systems are very important but have not been examined in terms of batch adsorber design. For these kinds of adsorbers, expensive materials, such as activated carbon, silica, and resins, are typically considered. Moreover, fresh adsorbent materials should be used in each stage. This disadvantage has turned the attention of researchers to low-cost materials such as industrial waste, which is easily available and efficient.

The best-fitted adsorption isotherm model was used to predict the design of single-stage, cross-flow, and counterflow batch adsorbers (Fig. 10) for the SST/Al–Cu nanocomposite.

Figs. 10a–c show the amount of adsorbent (*m*) required at an initial F⁻ concentration (C_0) of 5 mg L^{-1} for different volumes *V* (L). The Langmuir–Freundlich model gave the best fit for the equilibrium data from the SST/Al–Cu nanocomposite, and the equation for this model was used to predict the amount of nanocomposite required to adsorb 96%, 80%, and 70% from various volumes of fluoride solutions.

From Eq. (2), several linear plots were obtained for fluoride adsorption on SST/Al–Cu. The amount of nanocomposite required at different volumes, adsorption percentages, and initial concentrations is shown in Figs. 11a–g. For the three adsorber designs, a higher mass of SST/Al–Cu was used when the adsorption percentage was increased to 96% (Figs. 11a–c).

The counterflow adsorber needed a lower mass of nanocomposite to achieve 96% F⁻ removal. This system is generally considered to be the most economical and efficient because it requires a lower amount of adsorbent material and is environmentally sustainable due to the reuse of adsorbent materials in the process.

When C_0 increased (Figs. 11e–g), so did the amount of SST/Al–Cu, and the initial concentration was reduced until reaching 96% removal at different volumes. In the cross-flow system and for low initial concentrations (3 and 5 mg L^{-1}), the required nanocomposite decreased the final concentration to 0.2 mg L^{-1}. Similar behavior was observed in the counterflow system.

4. Conclusions

Al–Cu nanoparticles were supported onto SST and SSLP by a chemical reduction method. The presence of alloy, oxide, and hydroxide nanoparticles was confirmed by XRD, XPS, and EDS analysis. Solid wastes and nanocomposites were employed for F⁻ adsorption from aqueous solution. The method of synthesis affected the species of nanoparticles formed on both wastes. The textural, morphological and structural characteristics of SST and SSLP allowed the deposition of different amounts of nanoparticles on their surfaces. In both cases, the amount of Al was higher than that of Cu, but the proportions were different for SST and SSLP. The amount of Cu was higher in SST than in SSLP. The Al–Cu nanoparticles were deposited on the grain boundary of SST. The distribution of nanoparticles on the SS surface was heterogeneous. The process with SST/Al–Cu was best described with a pseudo-second-order model, indicating chemisorption through the sharing of electrons between the adsorbate and adsorbent by valence forces. Maximum adsorption was achieved in the first 100 min. The equilibrium time increased in the order of SSLP < SSLP/Al–Cu < SST < SST/Al–Cu. Multilinear plots were observed for the intraparticle diffusion model. Since the plot did not pass through the origin, intraparticle diffusion was not the only rate-controlling step. The best correlations were achieved for the Freundlich model (SST and SSLP waste), the Langmuir–Freundlich model (SST/Al–Cu nanocomposite) and the Redlich–Peterson model (SSLP/Al–Cu nanocomposite). The adsorption capacity increased in the order of SST, SSLP, SSLP/Al–Cu, and SST/Al–Cu. The maximum adsorption capacity of SST/Al–Cu (5.25 mg g^{-1}) was similar to the capacity of SSLP/Al–Cu (5.16 mg g^{-1}) from the Langmuir model. The modeling of single-stage, cross-flow, and counterflow batch adsorbers with SST/Al–Cu showed encouraging results, forecasting the good applicability of cross-flow and counterflow adsorbers for F⁻ removal from large volumes of polluted water.

References

[1] A. Khan, A. Rashid, R. Younas, R. Chong, A chemical reduction approach to the synthesis of copper nanoparticles, Int. Nano Lett., 6 (2016) 21–26.

[2] R. Chaiti, P. Tarasankar, Recent advances of metal–metal oxide nanocomposites and their tailored nanostructures in numerous catalytic applications, J. Mater. Chem. A, 5 (2017) 9465–9487.

[3] M. Manimaran, K. Kannabiran, Actinomycetes-mediated bio-genic synthesis of metal and metal oxide nanoparticles: progress and challenges, Lett. Appl. Microbiol., 64 (2017) 401–408.

[4] D.M. Clifford, C.E. Castano, J.V. Rojas, Supported transition metal nanomaterials: nanocomposites synthesized by ionizing radiation, Radiat. Phys. Chem., 132 (2017) 52–64.

[5] S.M. Prabhu, P. Koilraj, K. Sasaki, Synthesis of sucrose-derived porous carbon-doped $Zr_xLa_{1-x}OOH$ materials and their superior performance for the simultaneous immobilization of arsenite and fluoride from binary systems, Chem. Eng. J., 325 (2017) 1–13.

[6] L. Gomez-Hortigüela, A.B. Pinar, J. Perez-Pariente, T. Sani, Y. Chebude, I. Diaz, Ion-exchange in natural zeolite stilbite and significance in defluoridation ability, Microporous Mesoporous Mater., 193 (2014) 93–102.

[7] A. Vinati, B. Mahanty, S.K. Behera, Clay and clay minerals for fluoride removal from water: a state-of-the-art review, Appl. Clay Sci., 114 (2015) 340–348.

[8] L. Kuang, Y. Liu, D. Fu, Y. Zhao, FeOOH-graphene oxide nanocomposites for fluoride removal from water: acetate mediated nano FeOOH growth and adsorption mechanism, J. Colloid Interface Sci., 490 (2017) 259–269.

[9] S. Mishra, S. Daniele, Metal–Organic derivatives with fluorinated ligands as precursors for inorganic nanomaterials, Chem. Rev., 115 (2015) 8379–8448.

[10] A. Rađenović, J. Malina, T. Sofilić, Characterization of ladle furnace slag from carbon steel production as a potential adsorbent, Adv. Mater. Sci. Eng., 2013 (2013) 1–6.

[11] Y. Mohammed, C. Luqman, A.K. Moonis, T.S.Y. Choong, Adsorption of nickel on electric arc furnace slag: batch and column studies, Sep. Sci. Technol., 49 (2014) 388–397.

[12] M. Nilforoushan, S. Otroj, The study of ion adsorption by amorphous blast furnace slag, Iran. J. Chem., Eng., 34 (2015) 57–64.

[13] C. Sarkar, J. Kumar, S. Nath, Removal of Ni^{2+} ion from waste water by geopolymeric adsorbent derived from LD slag, J. Water Process Eng., 17 (2017) 237–244.

[14] X. Wang, G. Zhang, H. Lan, R. Liu, H. Liu, J. Qu, Preparation of hollow Fe-Al binary metal oxyhydroxide for efficient aqueous fluoride removal, Colloids Surf., A, 520 (2017) 580–589.

[15] H. Sadegh, G. Ali, V. Kumar, A. Makhlouf, R. Shahryari-Ghoshekandi, M. Nadagouda, M. Sillanpää, E. Megiel, The role of nanomaterials as effective adsorbents and their applications in wastewater treatment, J. Nanostruct. Chem. 7 (2017) 1–14.

[16] A.L. Srivastav, P.K. Singh, V. Srivastava, Y.C. Sharma, Application of a new adsorbent for fluoride removal from aqueous solutions, J. Hazard. Mater., 263 (2013) 342–352.

[17] A. Blanco-Flores, N. Arteaga-Larios, V. Pérez-García, M. Ojeda-Escamilla, I. Rodríguez-Torres, Efficient fluoride removal using Al-Cu oxide nanoparticles supported on steel slag industrial waste solid, Environ. Sci. Pollut. Res., 25 (2018) 6414–6428.

[18] A. Blanco-Flores, A. Colín-Cruz, E. Gutiérrez-Segura, V. Sánchez-Mendieta, D.A. Solís-Casados, M.A. Garrudo-Guirado, R. Batista-González, Efficient removal of crystal violet dye from aqueous solutions by vitreous tuff mineral, Environ. Technol., 35 (2014) 1508–1519.

[19] K.V. Kumar, K. Porkodi, Batch adsorber design for different solution volume/adsorbent mass ratios using the experimental equilibrium data with fixed solution volume/adsorbent mass ratio of malachite green onto orange peel, Dyes Pigm., 74 (2007) 590–594.

[20] A. Ballester, L.F. Verdeja, J. Sancho, Metalurgia extractiva, Fundamentos. Editorial Síntesis, Madrid, España, 2000.

[21] Md. Obaidullah, T. Furusawa, I.A. Siddiquey, M. Sato, N. Suzuki, Synthesis of $ZnO-Al_2O_3$ core-shell nanocomposite materials by fast and facile microwave irradiation method and investigation of their optical properties, Adv. Powder Technol., 28 (2017) 2678–2686.

[22] R. Bechara, A. Aboukäis, J.P. Bonnelle, X-ray photoelectron spectroscopic study of a Cu–Al–O catalyst under H_2 or CO atmospheres, J. Chem. Soc., Faraday Trans., 89 (1993) 1257–1262.

[23] S. Yokoyama, H. Takahashi, T. Itoh, K. Motomiya, K. Tohji, Synthesis of metallic Cu nanoparticles by controlling Cu complexes in aqueous solution, Adv. Powder Technol., 25 (2014) 999–1006.

[24] M. Seo, B. MacDougall, H. Takahashi, R.G. Kelly, Passivity and Localized Corrosion, Corrosion Division Ed., An International Symposium in Honor of Professor Norio Sato, Proceedings, United States of America, 1999, pp. 99–27.

[25] B.W. McMahon, J.P.L. Perez, J. Yu, J.A. Boatz, S.L. Anderson, Synthesis of nanoparticles from malleable and ductile metals using powder-free, reactant-assisted mechanical attrition, ACS Appl. Mater. Interfaces, 6 (2014) 19579–19591.

[26] Z. Yan, H. Yang, J. Ouyang, A. Tang, In situ loading of highly-dispersed CuO nanoparticles on hydroxyl-group-rich SiO_2-AlOOH composite nanosheets for CO catalytic oxidation, Chem. Eng. J., 316 (2017) 1035–1046.

[27] A. Blanco-Flores, V. Sánchez-Mendieta, E. Gutiérrez-Segura, A.R. Vilchis-Néstor, R.A. Morales-Luckie, Novel tuffite/Fe-Cu oxides nanocomposite with functionality for dye removal in aqueous solution, J. Environ. Chem. Eng., 4 (2016) 4472–4484.

[28] P.K. Khanna, S. Gaikwad, P.V. Adhyapak, N. Singh, R. Marimuthu, Synthesis and characterization of copper nanoparticles, Mater. Lett., 61 (2007) 4711–4714.

[29] M. Thommes, K. Kaneko, A.V. Neimark, J.P. Olivier, F. Rodriguez-Reinoso, J. Rouquerol, K.S.W. Sing, Physisorption of gases, with special reference to the evaluation of surface area and pore size distribution, Pure Appl. Chem., 87 (2015) 1051–1069.

[30] K.A. Mrinal, S. Asmita, M. Arnab, S. Shrabanee, D. Dhak, Removal of fluoride from drinking water using highly efficient nano-adsorbent, Al(III)-Fe(III)-La(III) trimetallic oxide prepared by chemical route, J. Alloys Compd., 719 (2017) 460–469.

[31] J. Zhao, Q. Huang, M. Liu, Y. Dai, J. Chen, H. Huang, X. Zhu, X. Zhang, Y. Wei, Synthesis of functionalized MgAl-layered double hydroxides via modified mussel inspired chemistry and their application in organic dye adsorption, J. Colloid Interface Sci., 505 (2017) 168–177.

[32] W. Feng-Chin, T. Ru-Ling, J. Ruey-Shin, Characteristics of Elovich equation used for the analysis of adsorption kinetics in dye-chitosan systems, Chem. Eng. J., 150 (2009) 366–373.

[33] A.S. Sartape, A.M. Mandhare, V.V. Jadhav, P.D. Raut, M.A. Anuse, S.S. Kolekar, Removal of malachite green dye from aqueous solution with adsorption technique using *Limonia acidissima* (wood apple) shell as low cost adsorbent, Arabian J. Chem., 10 (2017) S3229–S3238.

[34] S. Banerjee, M.C. Chattopadhyaya, Adsorption characteristics for the removal of a toxic dye, tartrazine from aqueous solutions by a low cost agricultural by-product, Arabian J. Chem., 10 (2017) S1629–S1638.

[35] B.H. Hameed, M.I. El-Khaiary, Malachite green adsorption by rattan sawdust: isotherm, kinetic and mechanism modeling, J. Hazard. Mater., 159 (2008) 574–579.

[36] W. Ma, Y. Chen, Performance and mechanism of Mg-Ca-Fe hydrotalcite-like compounds for fluoride removal from aqueous solution, J. Fluorine Chem., 200 (2017) 153–161.

[37] T. Wu, L. Mao, H. Wang, Adsorption of fluoride from aqueous solution by using hybrid adsorbent fabricated with Mg/Fe composite oxide and alginate via a facile method, J. Fluorine Chem., 200 (2017) 8–17.

[38] A. Verma, S. Kumar, S. Kumar, Statistical modeling, equilibrium and kinetic studies of cadmium ions biosorption from aqueous solution using *S. filipendula*, J. Environ. Chem. Eng., 5 (2017) 2290–2304.

[39] R. Saadi, Z. Saadi, R. Fazaeli, N.E. Fard, Monolayer and multilayer adsorption isotherm models for sorption from aqueous media, Korean J. Chem. Eng., 32 (2015) 787–799.

[40] J. Nyoo, A. Kurniawana, S. Ismadjia, Y.H. Ju, Nanocellulose based biosorbents for wastewater treatment: study of isotherm, kinetic, thermodynamic and reusability, Environ. Nanotech. Monitoring Manage. 8, (134–149) (2017).

[41] N. Ayawei, E.A. Newton, D. Wankasi, Modelling and interpretation of adsorption isotherms, J. Chem., 2017 (2017) 1–12.

[42] A. Bhatnagar, E. Kumar, M. Sillanpää, Fluoride removal from water by adsorption—A review, Chem. Eng. J., 171 (2011) 811–840.

[43] S. Kanrar, S. Debnath, P. De, K. Parashar, K. Pillay, P. Sasikumar, U.C. Ghosh, Preparation, characterization and evaluation of fluoride adsorption efficiency from water of iron-aluminium oxide-graphene oxide composite material, Chem. Eng. J., 306 (2016) 269–279.

[44] S. Ayoob, A.K. Gupta, Performance evaluation of alumina cement granules in removing fluoride from natural and synthetic waters, Chem. Eng. J., 150 (2009) 485–491.